J. Fluid Mech. (2002), *vol.* 459, *pp.* 187–206. © 2002 Cambridge University Press
DOI: 10.1017/S0022112002008030 Printed in the United Kingdom

Microchannels in series connected via a contraction/expansion section

By WING YIN LEE[1], MAN WONG[2] AND YITSHAK ZOHAR[1]†

[1]Department of Mechanical Engineering, Hong Kong University of Science and Technology, Clear Water Bay, Kowloon, Hong Kong

[2]Department of Electrical & Electronic Engineering, Hong Kong University of Science and Technology, Clear Water Bay, Kowloon, Hong Kong

(Received 13 March 2001 and in revised form 1 October 2001)

Fluid flow in microdevices consisting of pairs of microchannels in series was studied. The dimensions of the channels are about 40 μm × 1 μm × 2000 μm for the wide and about 20 μm × 1 μm × 2000 μm for the narrow channels. Pairs of wide and narrow channels, with integrated pressure sensors, are connected via transition sections with included angles varying from 5° to 180°. Minor pressure losses (not due to friction) were studied by passing nitrogen through the channels under inlet pressures up to 60 p.s.i. Each device was tested in the contraction mode, flow from wide to narrow channel, and in the opposite expansion mode, flow from narrow to wide channel. Mass flow rate was first measured as a function of the overall pressure drop. The detailed pressure distribution along the straight segments and around the transition section was then measured in order to understand the flow pattern. The Reynolds number for these flows is less than 1, suggesting the flow to be of the Hele-Shaw type with no separation such that the results for all the devices should be similar. However, the flow rate was found to decrease and the pressure loss to increase significantly with increasing included angle of the transition section, regardless of the flow direction. Flow separation due to the transition sections, if indeed there is any, cannot explain the large pressure drop since the kinetic energy is negligible.

1. Introduction

There is currently a rapid increase in the number of investigations into microfluidic systems. Since the micromachining techniques used to fabricate microdevices have been developed relatively recently, it is not surprising that very little is known about gas and liquid flow in microchannels. However, it is very important to understand fluid flows in microdomains in order to develop new and efficient microfluidic devices. Flows in microdomains are probably different from their counterparts in macrodomains, for which the Navier–Stokes equations can be applied. The issues to be addressed in the microdomain include: the determination of the length scale at which the continuum assumption breaks down; the modification of the macrodomain theories to account for non-continuum effects; and the assessment as to what extent phenomena such as flow separation, transition to turbulence and compressible effects (shock waves) still occur in microdomains (Ho & Tai 1998).

Flow through a straight channel is the simplest but most common configuration

† Author to whom correspondence should be addressed. mezohar@ust.hk

https://doi.org/10.1017/S0022112002008030 Published online by Cambridge University Press

in microfluidic systems. Accordingly, fluid flows in straight microchannels have been studied experimentally and theoretically (van den Berg, ten Seldam & van der Gulik 1993; Liu *et al.* 1993*b*; Harley *et al.* 1995; Wu *et al.* 1998). The measured mass flow rate and pressure distributions indicated the development of slip flow conditions. This flow field, however, presents a simple balance between pressure gradient and wall shear stress.

In addition to the major loss due to friction, there are minor losses due to a variety of elements such as bends, branching or contraction/expansion transitions in all internal fluidic systems. In many cases, the minor losses are negligible. Although in other cases, the minor losses cannot be neglected and are responsible for a large pressure drop. Thus, it is important to evaluate correctly the minor losses associated with various fluidic elements. For most common components, the use of theoretical analysis to predict the details of the head loss is very difficult. Consequently, head loss data for many standard elements in macrosystems are typically given in dimensionless forms based on empirical measurements (Benedict 1980). Similar data for microsystems are not available yet, and it is not obvious that the macrosystem results are directly applicable.

In microchannel systems, as in their macro counterparts, a variety of configurations are available to connect flow passages. In order to minimize pressure losses in microsystems, it is important to know whether the flow behaviour in the microdomain is similar to that observed in the macrodomain. Unexpected phenomena have been observed when dealing with fluidic microsystems (Ho & Tai 1998), and one of the most intriguing is flow separation. Flow separation may be geometric or dynamic. Geometric separation results when a fluid stream passes over a sharp corner and the fluid leaves the corner regardless of how much its velocity has been reduced by frictional effects. Typically, the Reynolds number is smaller than 1 for flows in microsystems with channel height on the order of 1 μm, suggesting that the flow is of the Hele-Shaw type with no separation even from sharp corners (Schlichting 1979). Beskok, Karniadakis & Trimmer (1996) calculated the shear-driven, grooved microchannel flow in an attempt to model the complex flow in a micromotor or a microbearing. They concluded that the flow had separated and started to recirculate in the grooves even for small Reynolds number flows. On the other hand, Santiago *et al.* (1998) used particle image velocimetry to demonstrate that the flow around a 30 μm wide obstacle captured many of the features of the low-Reynolds-number Hele-Shaw flow. The flow field in the 5 μm gap between the plates exhibited in-plane symmetry of motion with two stagnation points on either side of the cylindrical obstruction, and the classical wake was not observed since the flow was fully attached with no separation.

Recently, we have begun a systematic experimental study to evaluate the minor pressure loss in microchannel systems owing to bends (Lee, Wong & Zohar 2001*a*), gradual transitions (Lee *et al.* 2000), mixing (Lee *et al.* 2001*c*), and constriction elements (Li *et al.* 2000; Lee *et al.* 2001*b*). Initial results show that the flow resistance is higher than the friction loss, indicating that the flow may have separated at the sharp corners, and this additional resistance is not negligible although the channels are very long and the friction is very high. In the present work, microchannels connected in series via a variety of transition sections with gradual and sharp corners have been integrated with pressure microsensors not only to evaluate the minor loss but also to explore its origin.

2. Device design and fabrication

The microchannels and pressure microsensors were surface micromachined on silicon substrates. The dimensions of a wide channel are about 40 μm × 1 μm × 2000 μm,

https://doi.org/10.1017/S0022112002008030 Published online by Cambridge University Press

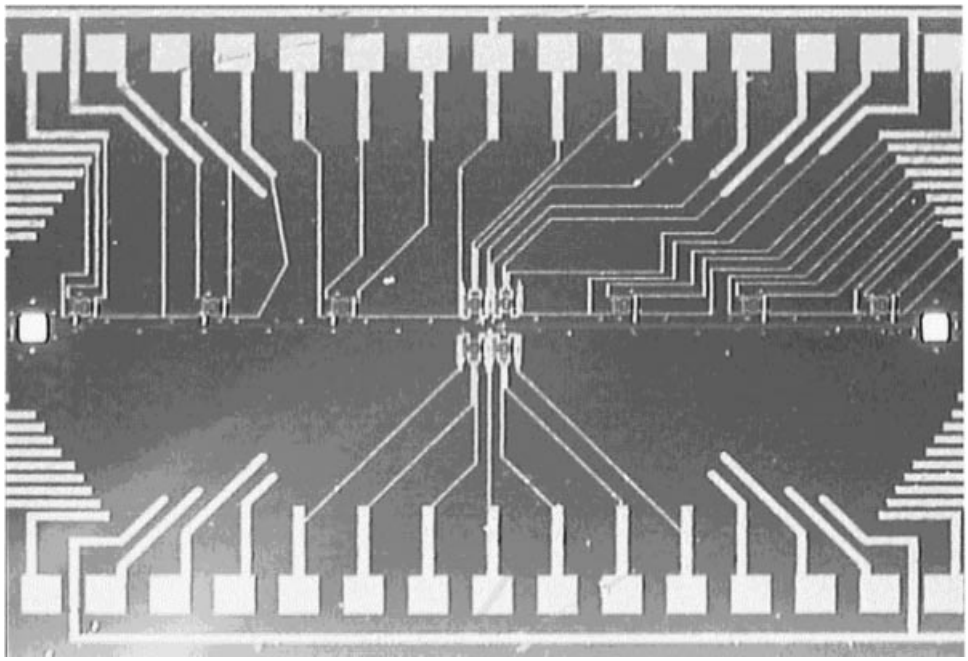


FIGURE 1. An overall picture of a fabricated device showing the pair of microchannels, transition section, pressure sensors, channel inlet/outlet, and metal interconnects.

and those of a narrow channel are about 20 μm × 1 μm × 2000 μm, as shown in figure 1. The narrow and wide channels in each pair are connected via a transition section with an included angle of 5°, 15°, 90° or 180°. The corresponding close-up pictures are shown in figure 2. Pressure sensors are sparsely distributed along the straight sections of the microchannel for reference, and densely around the transition sections. Each sensor is based on polycrystalline silicon piezoresistors arranged in a Wheatstone bridge configuration and attached to a membrane, 100 μm × 100 μm in size, as shown in figure 2. Any pressure difference across the membrane results in its deflection, thus straining the piezoresistors and changing their resistance. The voltage change due to the resistance change is recorded, and the pressure difference can be recovered using calibration curves.

Schematic cross-sections of the main fabrication steps are shown in figure 3. The fabrication started with the formation of a 0.15 μm thermal silicon dioxide and a 0.3 μm thick low-stress silicon nitride film on a silicon wafer for insulation. A 0.5 μm thick phosphosilicate glass (PSG) was deposited and patterned to form the channel and sensor chambers. This was followed by another deposition and patterning of a 0.5 μm thick PSG film. The pattern of the second PSG is similar to that of the first layer, except for the distributed pads along the sides of the patterns to be used as etching holes. The phosphorus content in the PSG determines the sacrificial layer etching-rate. The higher the phosphorus concentration, the faster is the etch rate (Liu *et al.* 1993*a*). In the present work, the phosphorus content was about 6%. Next, the structural layer of 1 μm low-stress silicon nitride was deposited and patterned to form the channel walls and ceiling as well as the sensor membranes (figure 3*a*). Orientation-dependent wet etching was used to create the inlet/outlet holes from the wafer underside, using the oxide/nitride insulating double layer as an etch mask.

https://doi.org/10.1017/S0022112002008030 Published online by Cambridge University Press

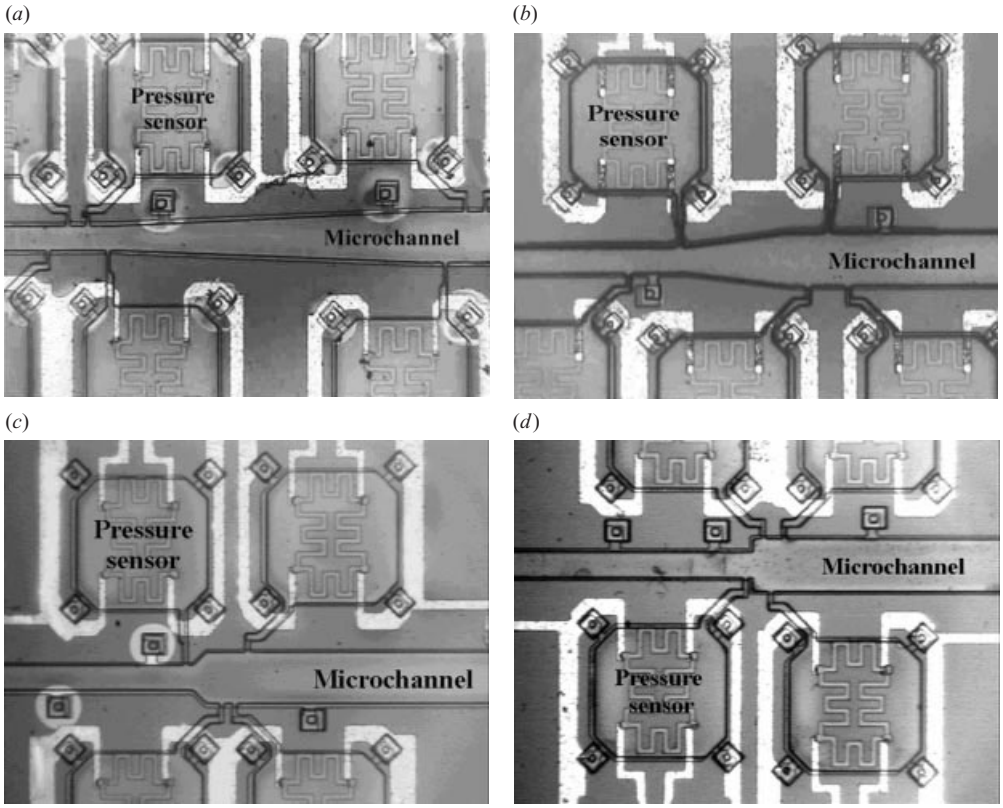


FIGURE 2. Close-up pictures of the transition section of the four tested devices with included angle of (*a*) 5°, (*b*) 15°, (*c*) 90°, and (*d*) 180°.

Following the opening of the etching holes, the PSG sacrificial layer was etched in 49% hydrofluoric acid (HF) (figure 3*b*). This step was critical as the release time could not be too long, since concentrated HF also etches silicon nitride at a rate of 0.04 μm min^{-1}. Therefore, the distance between adjacent etching holes should be designed properly. In the present work, the required time to release all the structures was less than 10 min. Then, a polysilicon layer of 0.5 μm in thickness was deposited, boron doped and patterned to form the piezoresistors (figure 3*c*) and to seal the etching holes. This process resulted in a very low pressure inside the sealed chambers, and the diaphragms were deflected downward under ambient atmospheric pressure. A 1 μm thick aluminium layer for interconnections was sputter deposited, patterned and sintered. Finally, the fabrication process was completed with the etching of the polysilicon and silicon nitride films separating the microchannels from the inlet/outlet holes (figure 3*d*).

3. Experimental set-up

The experimental set-up is shown in figure 4. Nitrogen gas was passed through the microdevices under inlet pressure of up to 60 p.s.i. at room temperature of 20 °C, and the flow rate was measured using a glass syringe with a volume of 10 μl. The volume flow rate was determined visually as a meniscus of water travelled past the marked scale on the syringe as a function of time. Multiplying this rate by the outlet

https://doi.org/10.1017/S0022112002008030 Published online by Cambridge University Press

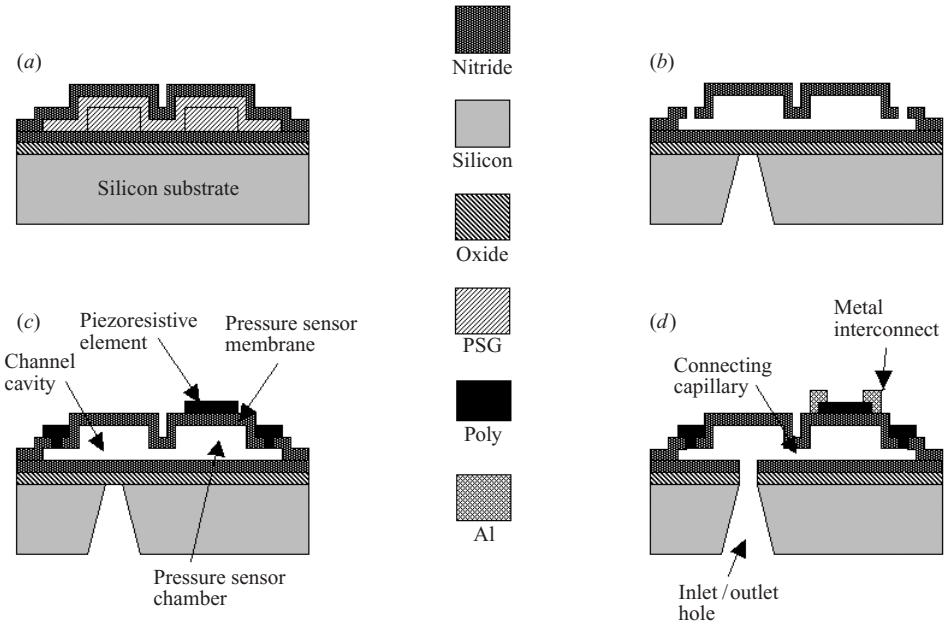


FIGURE 3. Cross-sections of the major fabrication steps.

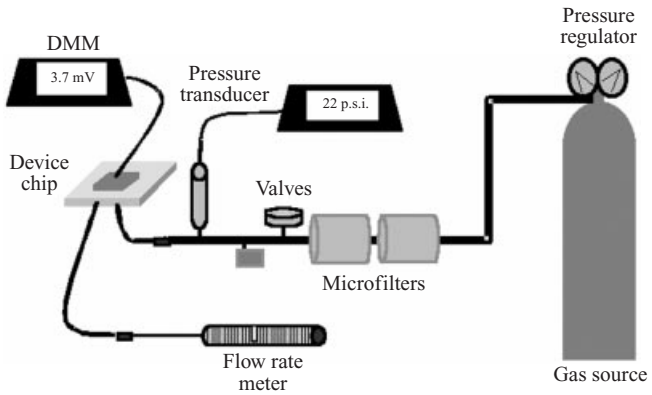


FIGURE 4. The experimental set-up.

gas density of 1 atm yields the mass flow rate. Repeated measurements under the same conditions revealed that the relative experimental error is about $\pm 2.5\%$ of the nominal value. The contraction and expansion experiments were carried out in the same device by reversing the flow direction.

During the sacrificial layer etching to create the channel cavity, the nitride films forming the upper and lower solid boundaries were also slightly etched. This results in a channel height larger than the sacrificial-layer thickness. Since the flow rate is a cubic function of the channel height, it is very important to find out its value as accurately as possible. The mass flow rate in a straight and uniform microchannel under a given pressure drop, $\Delta P = P_i - P_o$, can be calculated as follows (Arkilic,

https://doi.org/10.1017/S0022112002008030 Published online by Cambridge University Press

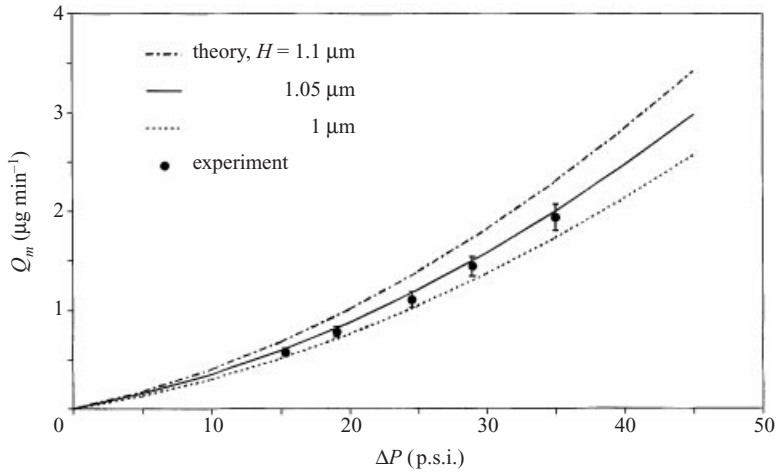


FIGURE 5. A comparison between calculated and measured mass flow rates for a straight, uniform microchannel to determine the channel height that provides the best fit.

Schmidt & Breuer 1997):

$$Q_m = \frac{H^3 W P_o^2}{24RTL\mu}\left[\left(\frac{P_i}{P_o}\right)^2 - 1 + 12Kn_o\left(\frac{P_i}{P_o} - 1\right)\right], \tag{1}$$

where H, W and L are the channel height, width and length; P_i and P_o are the inlet and outlet pressure; T, μ and R are the fluid temperature, viscosity and specific gas constant, respectively; $Kn_o = \lambda_o/H$ is the outlet Knudsen number based on the outlet mean free path, λ_o. In the present experiments, $Kn_o = 0.06$ for nitrogen at an exit pressure of 1 atm. This model accounts for compressible and slip-flow effects, but neglects acceleration and non-parabolic velocity profile effects (van den Berg *et al.*). Equation (1) has been shown to provide good predictions of mass flow rate in a straight microchannel (Wu *et al.* 1998); hence, it can be used to determine the effective channel height. Alongside a microchannel pair with a transition section, a uniform microchannel was also fabricated simultaneously on the same wafer. The measured mass flow rate for the straight channel is compared with a family of curves calculated from equation (1) for different heights, as shown in figure 5. The height corresponding to the best fit of the analytical calculations to the experimental measurements, $H = 1.05$ μm, is the best available estimate of the actual channel height. Since the microchannel pair was fabricated following an identical process flow, we assume that the height of both the uniform and the non-uniform microchannels are the same. The highest mass flow rate recorded in the present experiments is about 2.5 μg min^{-1} with maximum average speed of 1.75 m s^{-1}. Thus, the Reynolds number is of the order of 0.1, and the Mach number is less than 0.005.

4. Mass flow rate measurements and calculations

Flow rate measurements were conducted to assess the effect of the transition sections on the overall fluid flow. In an attempt to provide a theoretical reference for this assessment, the flow rate through a non-uniform microchannel is first calculated assuming the flow is fully attached everywhere.

https://doi.org/10.1017/S0022112002008030 Published online by Cambridge University Press

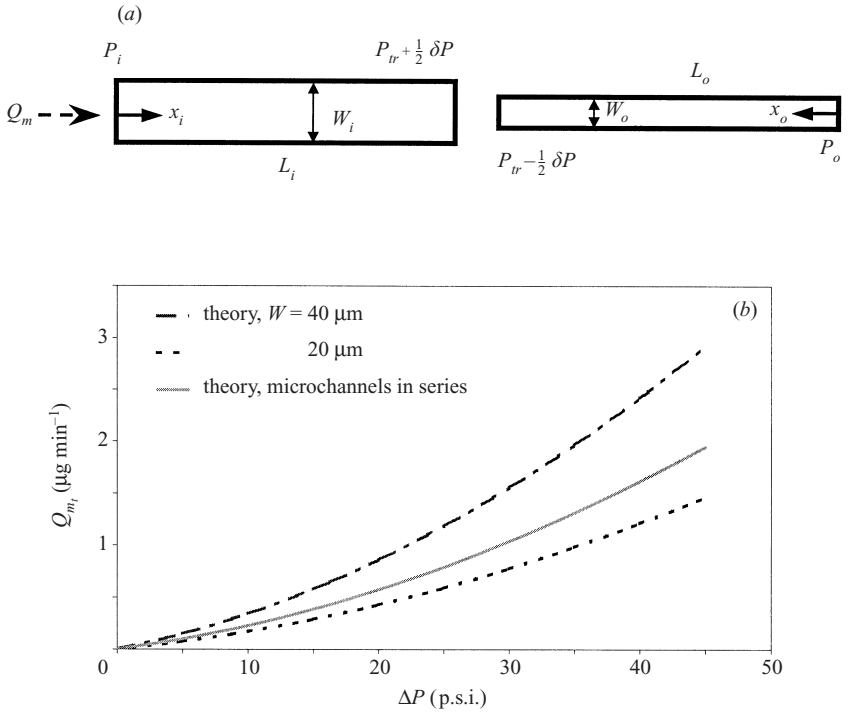


FIGURE 6. Theoretical calculations of mass flow rate for a microchannel pair connected in series assuming fully attached flow: (*a*) physical model, and (*b*) analytical results.

4.1. *Mass flow rate calculations under the fully attached flow assumption*

Since the cross-section area of a microchannel pair is not uniform along its entire length, equation (1) cannot be used to provide theoretical predictions. However, the cross-section of each channel segment between the transition section and either the channel inlet or the channel outlet is uniform. Consequently, assuming there is no pressure loss due to a transition section, equation (1) can be applied to the upstream and downstream channels as follows:

$$Q_{m_i} = \frac{H^3 W_i (P_{tr} + \delta P/2)^2}{24RTL_i\mu}\left[\left(\frac{P_i}{P_{tr}+\frac{1}{2}\delta P}\right)^2 - 1 + 12Kn_{tr}\left(\frac{P_i}{P_{tr}+\frac{1}{2}\delta P} - 1\right)\right], \tag{2a}$$

$$Q_{m_o} = \frac{H^3 W_o P_o^2}{24RTL_o\mu}\left[\left(\frac{P_{tr}-\frac{1}{2}\delta P}{P_o}\right)^2 - 1 + 12Kn_o\left(\frac{P_{tr}-\frac{1}{2}\delta P}{P_o} - 1\right)\right], \tag{2b}$$

where the subscripts '*i*' and '*o*' refer to the uniform channels connecting the device inlet and outlet to the transition section, respectively. The terms P_{tr} and δP are the average and the difference between the pressure at the outlet of the upstream channel and at the inlet of the downstream channel, as sketched in figure 6(*a*). The length of each channel segment is identical, $L_i = L_o = \frac{1}{2}L = 2000\,\mu$m, and the height is uniform, $H = 1.05\,\mu$m, as determined in § 3. The channel width is either $W_i = 2W_o = 40\,\mu$m or $W_i = \frac{1}{2}W_o = 20\,\mu$m for the contraction or expansion

https://doi.org/10.1017/S0022112002008030 Published online by Cambridge University Press

modes, respectively. Conservation of mass requires $Q_{m_i} = Q_{m_o} = Q_m$, and combining equations 2(a) and 2(b) yields a single equation with one unknown, P_{tr}. The Knudsen number at the transition section, Kn_{tr}, does not constitute an extra unknown since it can be expressed in terms of the other parameters, $Kn_{tr}P_{tr} = Kn_oP_o$ (Arkilic *et al.* 1997). The term δP can be estimated using conservation of mass and energy across the transition section assuming no pressure loss. The mass flow rate through the microchannel pair is calculated by solving for P_{tr} and using either 2(a) or 2(b). In this model, the outlet of the upstream and the inlet of the downstream sections are considered to be open to an ambient pressure of P_{tr}, whereas in reality each is restricted by the adjacent section. However, since the channels are very long compared to the hydraulic diameter and the velocities are very low, these end effects are very small and can be neglected.

The dynamic pressure in the current microsystem is very small compared with the driving pressure drop. Hence, the calculated pressure difference across the transition section δP due only to the area change is very small, $\delta P/\Delta P < 10^{-5}$. Consequently, flow reversal should result in similar flow rates, as shown in figure 6(b), for both contraction and expansion modes. The calculated mass flow rate is compared with the rate through uniform channels having the same overall length of 4000 μm and width the same as either the wide, 40 μm, or narrow channel, 20 μm. As expected, the mass flow rate calculated for the channel pair is higher than the narrow and lower than the wide channel flow rate. These calculations will provide the basis for comparison with measurements to determine whether the transition section has an effect on the overall flow behaviour.

4.2. *Mass flow rate measurements*

Mass flow rate was measured as a function of the pressure drop, in both contraction and expansion modes, and the results are summarized in figures 7(a) and 7(b) for the devices with an included angle of 5° and 180°, respectively. In all cases, the flow rate of the expansion mode is about equal to or slightly smaller than the flow rate of the contraction mode. This is in contrast to macrofluidic systems where the loss in converging flow is appreciably smaller than in diverging flow, since flow acceleration is a much more efficient process than flow deceleration.

A comparison between the flow rate through all the devices in either contraction or expansion mode is shown in figures 8(a) and 8(b), respectively. In each mode, the flow rate decreases monotonically with increasing included angle over the entire pressure-drop range tested. Such consistent results indicate that it is more likely that this behaviour is not a result of inherent random system errors, but rather a true effect of the transition section on the gas flow through the microchannel.

The mass flow-rate dependence on the included angle of the transition section is summarized in figure 9 for both contraction and expansion modes. The measured mass flow rate drops monotonically from close to 100% of the theoretical value for the 5°-included angle to about 65% for the 180°-included angle device. It is plausible that the monotonic decrease of the flow rate is only an artefact of having tested four angles only, and with more transition angles the curve could have been quite different with local maximum and minimum as in macrofluidic systems. The mass flow rate of the expansion is marginally lower than that of the contraction mode, except for the 90°-included angle device for which the difference is larger. This is quite different from macrosystems, where contraction sections result in significantly smaller losses than expansion sections.

https://doi.org/10.1017/S0022112002008030 Published online by Cambridge University Press

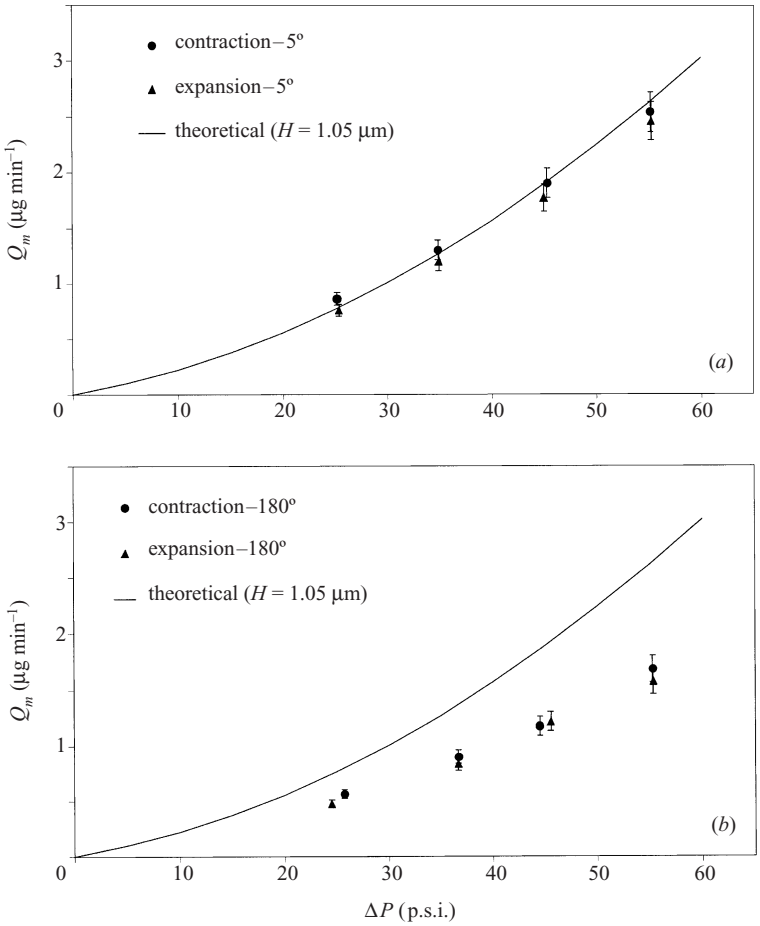


FIGURE 7. Mass flow rate measurements in both contraction and expansion modes for the devices with included angle of (*a*) 5°, and (*b*) 180°.

5. Pressure distribution measurements and calculations

Prior to the pressure distribution measurements, all sensors were calibrated. The inlets and outlets of each device were connected to the gas source to ensure uniform pressure within the entire device. The pressure was then adjusted, and once a steady state was reached the voltage output of all sensors was recorded. The process was repeated 6–8 times, for different pressure levels, until satisfactory calibration curves were obtained as depicted in figure 10(*a*). Although every device includes 10 or 11 sensors, it is rare to find a device for which all the sensors are in good working order. Sensors can malfunction owing to either imperfect fabrication processes or difficulties in packaging. In order to estimate the experimental error in the pressure measurements, the calibration process was repeated independently by different users on different dates, as shown in figure 10(*b*). The peak-to-peak pressure fluctuations, P_{pp}, are typically about 6% of the average pressure across the membrane, ΔP, i.e. relative experimental error of $\pm 3\%$. However, the relative error of the worst sensor was about $\pm 5\%$, and this should be taken as the uncertainty of all pressure measurements. Calculations of the pressure distribution are first performed to provide a reference for the experimental data.

https://doi.org/10.1017/S0022112002008030 Published online by Cambridge University Press

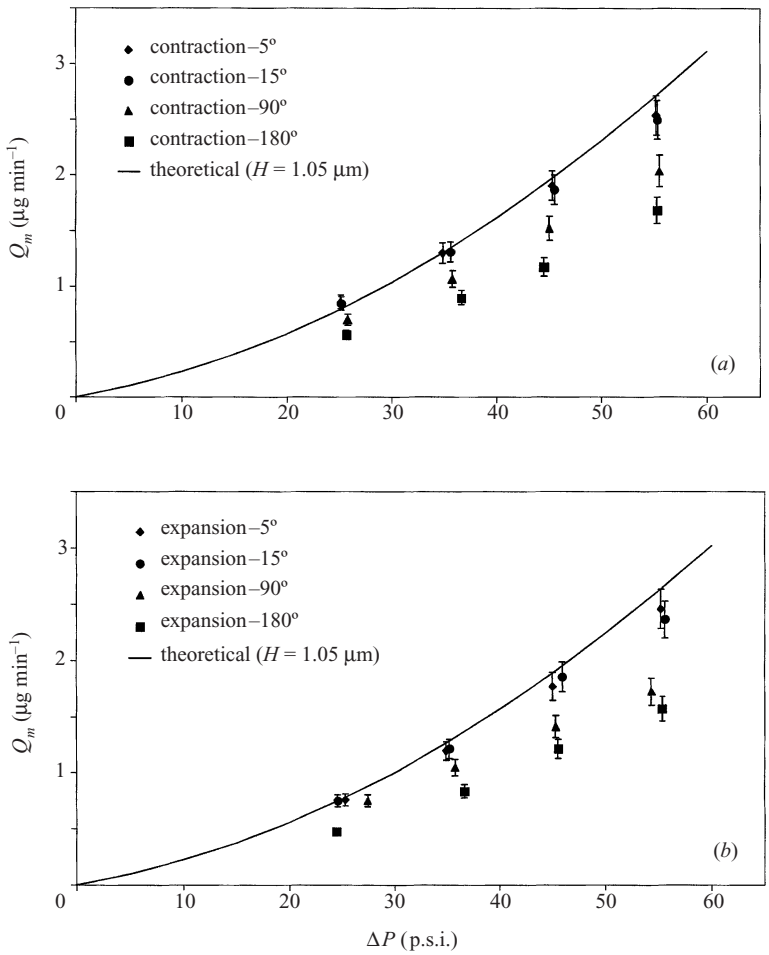


FIGURE 8. A comparison between the measured mass flow rate for the four included angles in (*a*) contraction, and (*b*) expansion modes.

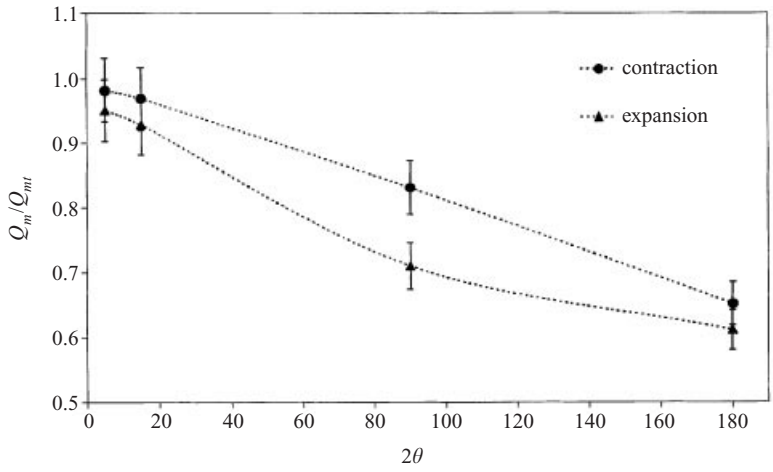


FIGURE 9. Mass flow-rate dependence on the included angle of the transition section.

https://doi.org/10.1017/S0022112002008030 Published online by Cambridge University Press

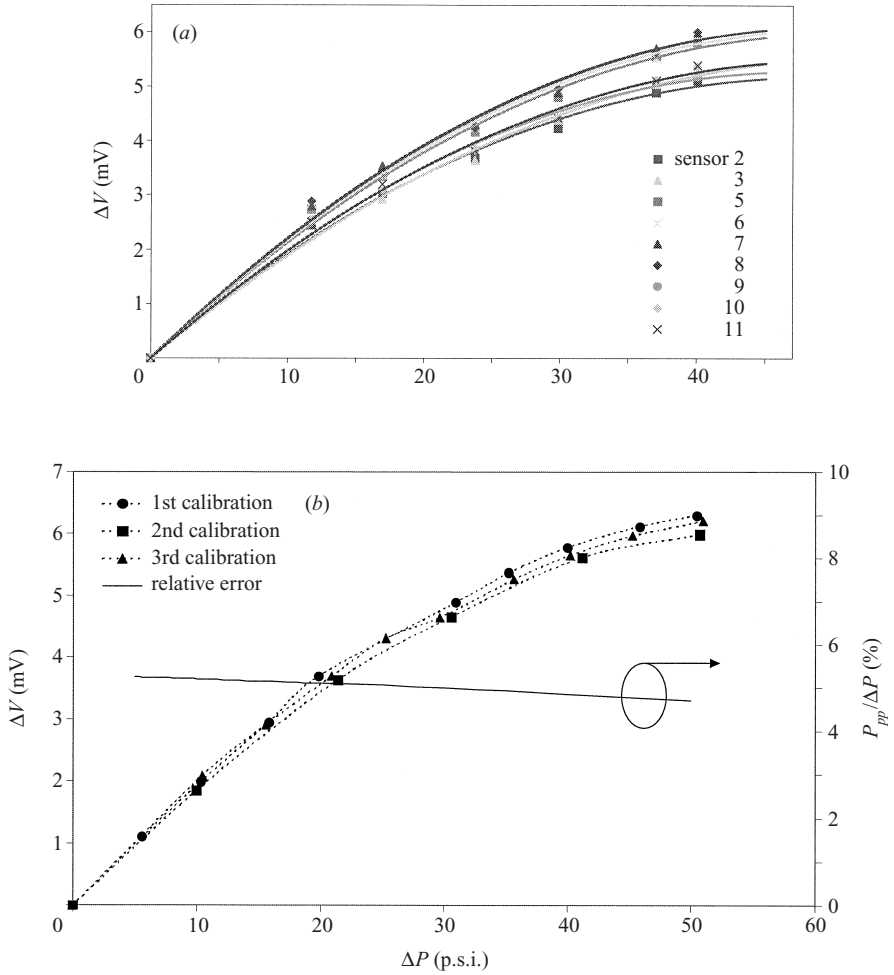


FIGURE 10. Pressure sensor calibration: (*a*) calibration curves of the sensors of the 15°-included angle device, and (*b*) repeated calibrations of a single sensor.

5.1. *Pressure distribution calculations along the non-uniform microchannel*

The analytical model applied for calculating the mass flow rate in equation (1) can also be used to predict the pressure distribution $P(x)$ along a straight, uniform microchannel (Arkilic *et al.* 1997):

$$\frac{P(x)}{P_o} = -6Kn_o + \left\{\left(6Kn_o + \frac{P_i}{P_o}\right)^2 - \left[\left(\frac{P_i^2}{P_o^2} - 1\right) + 12Kn_o\left(\frac{P_i}{P_o} - 1\right)\right]\left(\frac{x}{L}\right)\right\}^{1/2}. \tag{3}$$

The corresponding profile for $\Delta P = 50$ p.s.i. is shown as the dashed line in figure 11. The current device consists of a pair of microchannels with different width and, hence, it is not straightforward to apply equation (3). However, under the attached flow assumption discussed in § 4.1, the pressure distribution can be calculated piecewise

https://doi.org/10.1017/S0022112002008030 Published online by Cambridge University Press

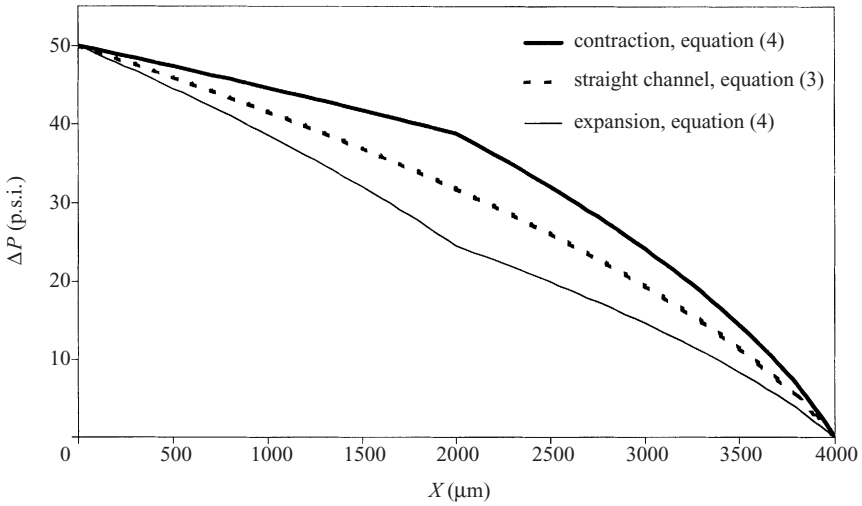


FIGURE 11. Calculated streamwise pressure distributions for a uniform and a non-uniform straight microchannel.

for each straight section by using P_{tr} and neglecting δP, since $\delta P/P_{tr} \sim 10^{-5}$:

$$\frac{P(x)}{P_{tr}} = -6Kn_{tr} + \left\{\left(6Kn_{tr} + \frac{P_i}{P_{tr}}\right)^2 - \left[\left(\frac{P_i^2}{P_{tr}^2} - 1\right) + 12Kn_{tr}\left(\frac{P_i}{P_{tr}} - 1\right)\right]\left(\frac{x}{L_i}\right)\right\}^{1/2}, \tag{4a}$$

$$\frac{P(x)}{P_0} = -6Kn_o + \left\{\left(6Kn_o + \frac{P_{tr}}{P_o}\right)^2 - \left[\left(\frac{P_{tr}^2}{P_o^2} - 1\right) + 12Kn_o\left(\frac{P_{tr}}{P_o} - 1\right)\right]\left(\frac{x}{L_o}\right)\right\}^{1/2}, \tag{4b}$$

where 4(a) is applied to the upstream and 4(b) to the downstream straight section. The calculated pressure distributions for both modes, contraction and expansion, are compared with the straight channel profile in figure 11. Although the mass flow rate under the same pressure drop is identical for both modes, contraction and expansion, the pressure distribution is not similar since the pressure loss due to friction in the narrow section is significantly higher than the loss in the wide section. The straight-channel distribution is about the average of the two modes. The calculated pressure distributions will be tested against experimental results.

5.2. *Pressure distribution measurements along the channel straight sections*

Pressure measurements were collected for all devices under three flow-rate levels for either the contraction or the expansion mode. The results for the contraction and expansion mode are summarized, respectively, in figures 12(a) and 12(b) for the 15°-included angle device, of which all the sensors functioned properly. As expected, the pressure gradient along the narrow section, whether it is next to the inlet or the outlet, is higher than the gradient along the wide section owing to the higher frictional loss. Furthermore, the pressure distributions through the transition section are not continuous as the calculated distributions shown in figure 11. Instead, a sharp drop immediately downstream of the transition section is evident. Extrapolation

https://doi.org/10.1017/S0022112002008030 Published online by Cambridge University Press

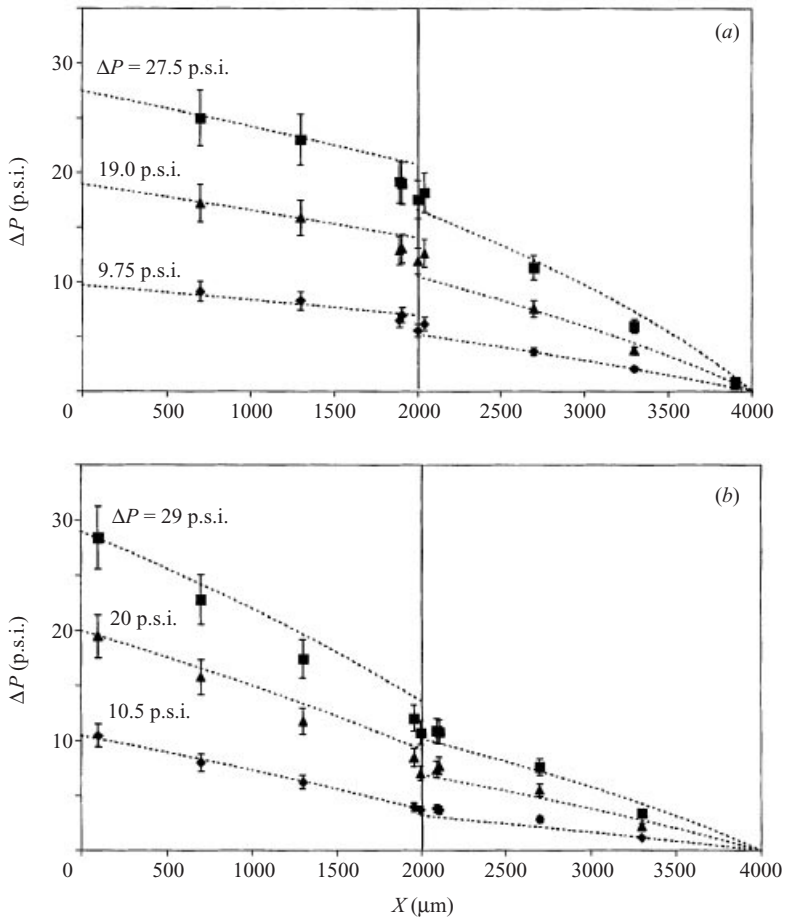


FIGURE 12. Streamwise pressure distributions along the 15°-included angle device in (*a*) the contraction, and (*b*) the expansion modes.

of the pressure measurements from either the inlet or the outlet to the transition section provides an estimate of the pressure upstream, P_{u_o}, and downstream, P_{d_i}, of the transition section. Then, replacing P_{tr} with P_{u_o} in 4(*a*) and with P_{d_i} in 4(*b*), the pressure distribution along the upstream and downstream straight segments can be calculated. The results shown in figure 12 as dashed lines agree well with the experimental measurements. This indicates that along the straight sections, away from the transition section and the channel inlet and outlet, the gas flow develops like flow along a straight and uniform microchannel.

5.3. *Minor pressure loss due to the transition section*

The difference between the static pressure upstream and downstream of the transition section, $\Delta P_m = P_{u_o} - P_{d_i}$, cannot be attributed to frictional loss within the physically small dimension of the transition section, especially for the 180°-included angle device. Therefore, it should be classified as minor pressure loss due to the transition section. The estimated pressure loss for the tested devices is plotted in figures 13(*a*) and 13(*b*) as a function of the mass flow rate for the contraction and expansion modes, respectively. The loss increases monotonically, though not linearly, with the mass

https://doi.org/10.1017/S0022112002008030 Published online by Cambridge University Press

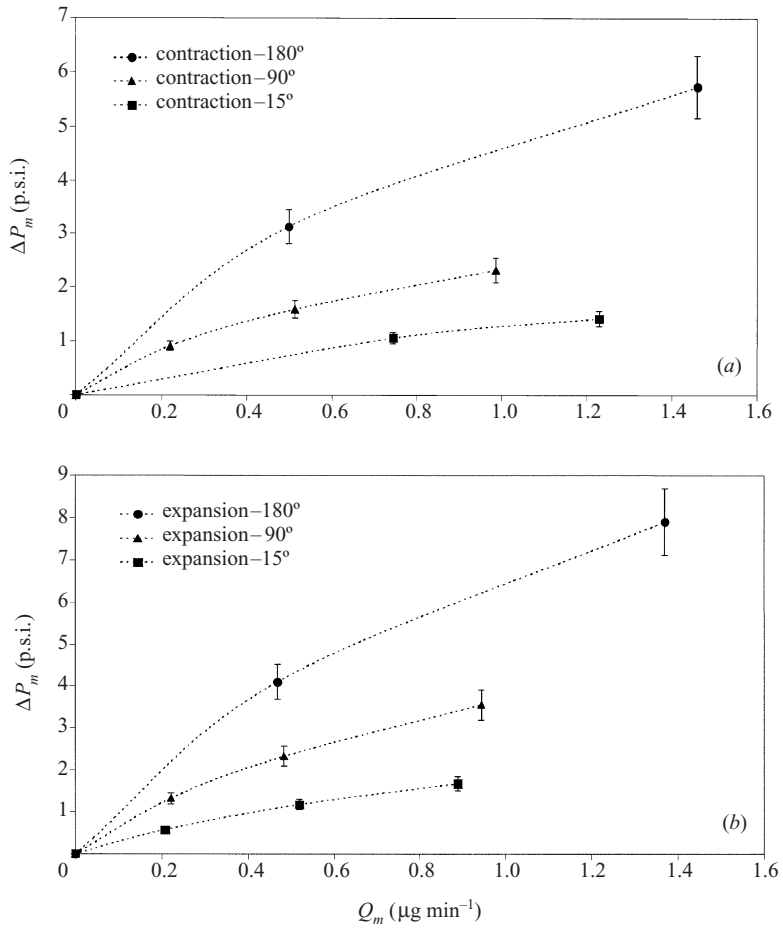


FIGURE 13. Pressure loss as a function of the mass flow rate due to (*a*) the contraction, and (*b*) the expansion sections.

flow rate. The loss for the 5°-included angle device is practically zero and, hence, is not shown. Accounting for this additional pressure loss, the calculated flow rates can be corrected. The pressure loss cannot be simply either deducted from the inlet pressure or added to the outlet pressure, since not only is the pressure distribution nonlinear, but also the channel cross-section is not uniform. To correct the predicted flow rate shown in figure 6(*b*), δP should be replaced by ΔP_m in equations 2(*a*) and 2(*b*). Indeed, the corrected calculations summarized in figures 14(*a*) and 14(*b*) for the contraction and expansion modes agree well with the mass flow rate measurements.

In macrofluidic systems, it is very difficult to predict minor losses analytically. Consequently, they are usually given in dimensionless form, based on experimental data. The most common method used to determine the loss coefficient, K_L, is to normalize the pressure loss by the dynamic pressure as follows:

$$K_L = \frac{\Delta P_m}{\frac{1}{2}\rho_n V_n^2}, \tag{5}$$

where ρ_n and V_n are the density and average velocity, respectively, in the narrow channel immediately next to the transition section. However, surface forces are so

https://doi.org/10.1017/S0022112002008030 Published online by Cambridge University Press

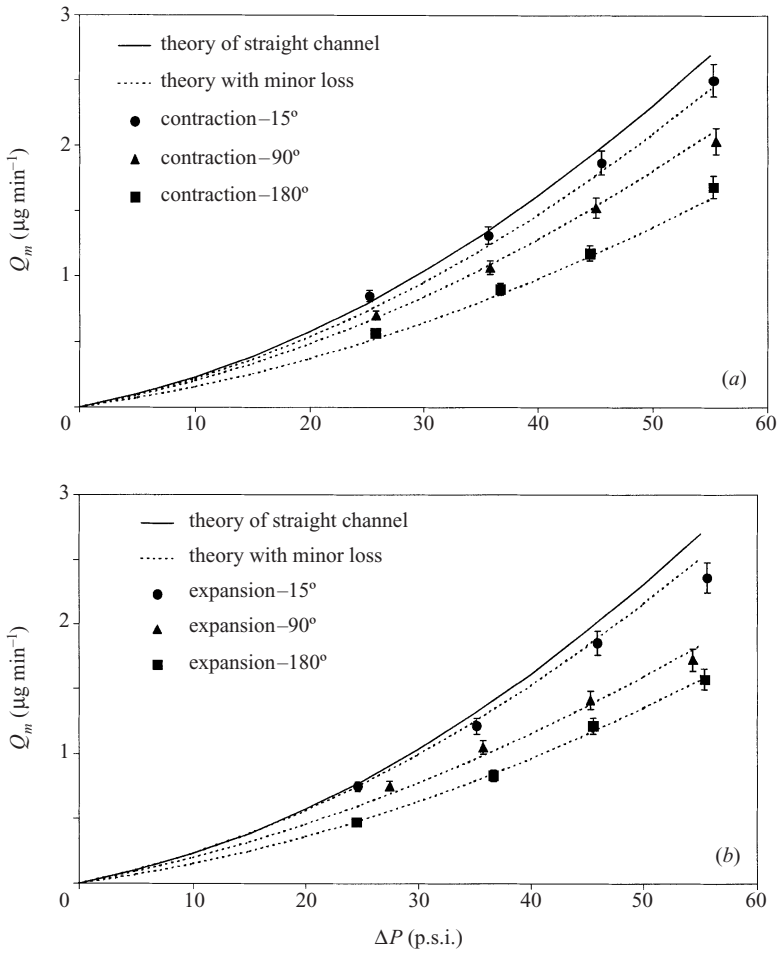


FIGURE 14. A comparison between the measured and corrected calculations of mass flow rate accounting for pressure loss due to (*a*) the contraction, and (*b*) the expansion sections.

dominant in microfluidic systems that the dynamic pressure is in most cases very small. Hence, the calculated loss coefficient for the current microsystems based on equation (5) is very large and of the order of 10^{11}. It is more appropriate then to normalize the minor pressure loss with the major loss due to friction, given in terms of an equivalent length L_e. In this terminology, the pressure loss due to the transition section, $P_{u_o} - P_{d_i}$, is expressed by an equivalent length of the microchannel that would produce the same pressure loss as the transition section, as follows:

$$Q_m = \frac{H^3 W_{tr} P_{d_i}^2}{24RTL_e\mu}\left[\left(\frac{P_{u_o}}{P_{d_i}}\right)^2 - 1 + 12Kn_{tr}\left(\frac{P_{u_o}}{P_{d_i}} - 1\right)\right]. \tag{6}$$

Since the pressure distribution is nonlinear, the equivalent channel length has to be inserted at the location of the transition section. Furthermore, the microchannel width is not constant, hence the width of the equivalent length section is selected to be the average width, $W_{tr} = \frac{1}{2}(W_i + W_o) = 30\,\mu\text{m}$, as illustrated in figure 15(*a*). Thus, for any given flow rate through any device, the pressure upstream and downstream of the transition section can be estimated and, subsequently, the equivalent length can

https://doi.org/10.1017/S0022112002008030 Published online by Cambridge University Press

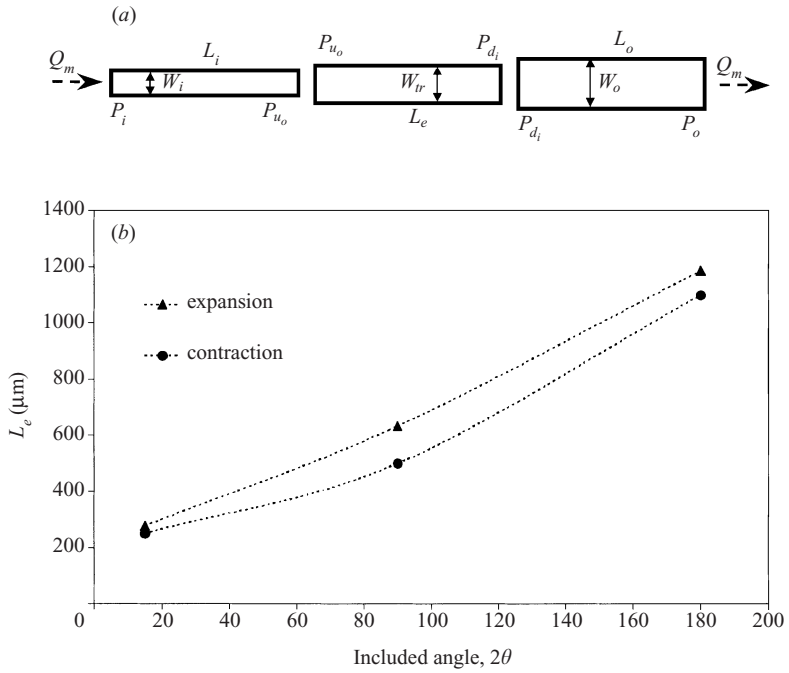


FIGURE 15. Equivalent-length dependence on the included angle of the transition section: (*a*) physical model, and (*b*) empirical calculations (equation (6)).

be calculated based on equation (6). The results are plotted in figure 15(*b*), where the equivalent length increases monotonically with the included angle with little difference between the contraction and expansion mode. The equivalent length increases from about 200 μm for the 15°-included angle to just over 1000 μm for the 180°-included angle device, which is about 25% of the overall channel length. Clearly, this is a more reasonable approach to characterize the minor loss due to the transition section.

5.4. *Pressure distributions around the transition section*

Pressure distributions around the transition sections could be used to construct the flow pattern around these sections and, subsequently, shed light on the origin of the minor pressure loss. The experimental results are shown in figures 16 and 17 for the contraction and expansion mode, respectively. Evidently, the available data points are not sufficient to obtain a continuous distribution through the entire transition section, since the size of the sensor membrane limits the number of sensors (less than 5) that could be integrated around this short region. Nevertheless, some features could still be discerned from the present measurements.

The static pressure decreases through the contraction section as expected with decreasing flow area and increasing average velocity. However, the pressure increases slightly immediately downstream of the 15°-included angle contraction (figure 16*a*) rather than continuing to decrease owing to friction. Unfortunately, the corresponding sensor in the 180°-included angle contraction did not function (figure 16*b*), though the analytical extrapolation shows similar trend. This means that the maximum pressure downstream of the contraction section is not obtained at the starting point of the narrow straight segment, as should be the case for fully attached flow. In the expansion mode, if the flow is fully attached, the pressure should increase monotonically through

https://doi.org/10.1017/S0022112002008030 Published online by Cambridge University Press

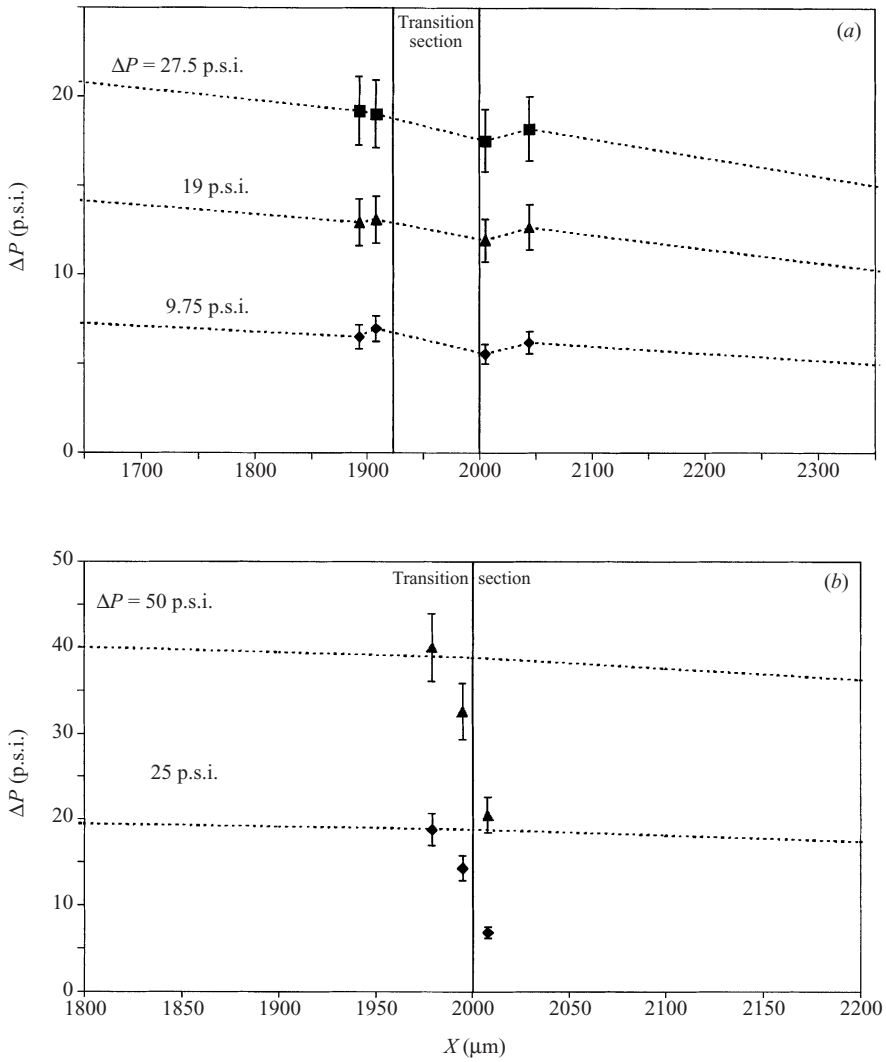


FIGURE 16. Detailed pressure distributions around the contraction section with included angle of (*a*) 15°, and (*b*) 180°.

the transition section and reach the maximum level at the starting point of the wide straight section. However, the pressure either decreases or stays the same through the transition sections (figure 17). Furthermore, the pressure increases slightly immediately downstream of the 180°-included angle expansion, (figure 17*b*), before decreasing owing to friction. Again, the maximum pressure is not obtained at the initial point of the wide straight segment, suggesting that the flow may not be fully attached.

6. Flow patterns

Flow visualization is an indispensable tool to obtain reliable flow patterns, which, in turn, can help in the understanding of the physics of fluid motion. The application of optical methods to analyse fluid flows in internal microsystems is still in its infancy (Meinhart, Wereley & Santiago 1999). Therefore, indirect measurements such

https://doi.org/10.1017/S0022112002008030 Published online by Cambridge University Press

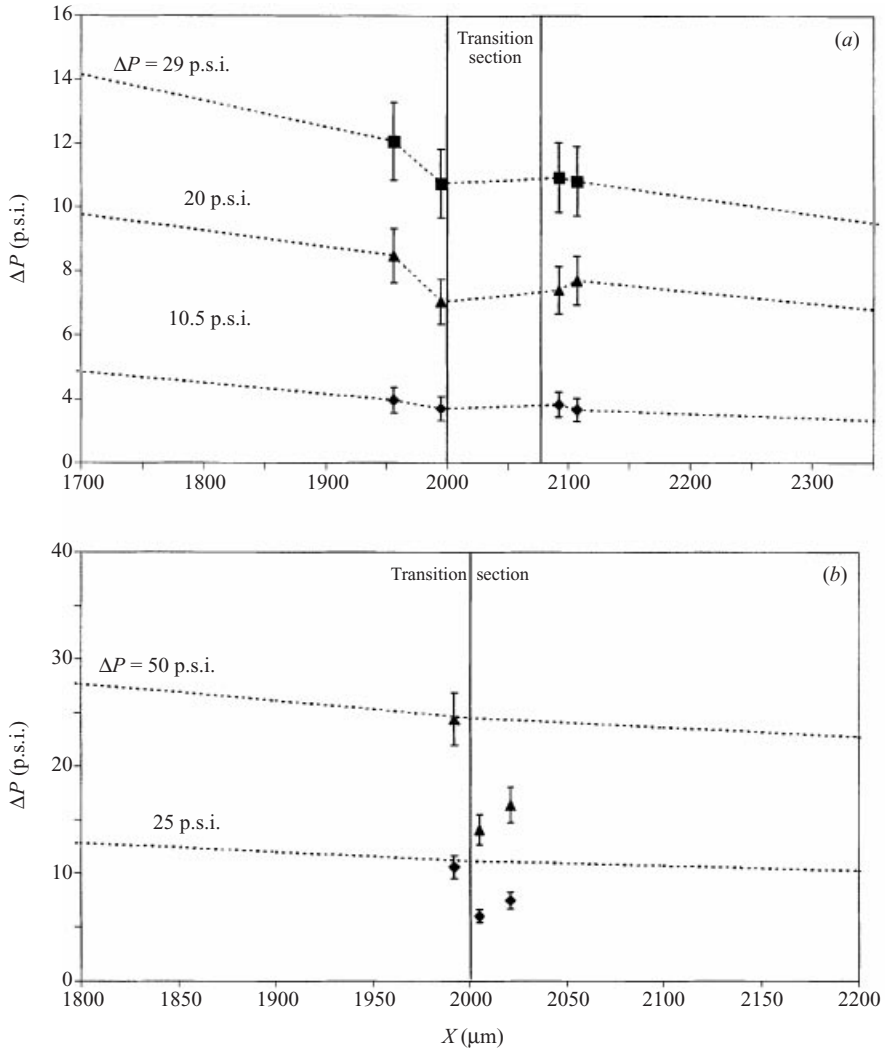


FIGURE 17. Detailed pressure distributions around the expansion section with included angle of (*a*) 15°, and (*b*) 180°.

as pressure distributions could prove to be critical. It is tempting to interpret the peculiar pressure distributions around the transition sections as a result of flow separation from the sharp corners of these sections, as illustrated in figure 18, in an effort to explain the pressure loss. In such a scenario, the flow downstream of a contraction section continues to converge forming a vena contracta before diverging to fill up the entire cross-section of the narrow channel (figure 18*a*). The minimum pressure is obtained at the vena contracta, as in a macrosystem, and the static pressure should increase slightly before the expected decrease due to friction. Similarly, the flow downstream of an expansion section separates from the sharp corners and converges gradually to fill the cross-section of the wide channel (figure 18*b*). The maximum static pressure is obtained at the reattachment point and not at the start of the wide section, which is consistent with some observations.

Indeed, flow separation in a macrosystem always results in pressure loss either

https://doi.org/10.1017/S0022112002008030 Published online by Cambridge University Press

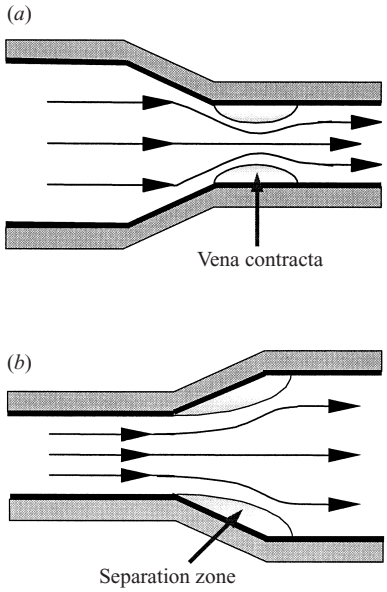


FIGURE 18. Possible flow patterns around (*a*) the contraction, and (*b*) the expansion sections, based on the flow rate and pressure distribution measurements.

to maintain secondary flows, such as vortices, or due to energy dissipation in the separated zones. In the transition sections, this loss is at the expense of the kinetic energy of the primary flow resulting in smaller pressure recovery. Although termed a minor loss, the pressure loss could be very significant if the kinetic energy is high compared with the overall pressure drop, as in most macrosystems. However, in microsystems the kinetic energy is usually extremely small compared to the large pressure drop required to maintain the flow against friction. Therefore, even if the entire kinetic energy is lost within the transition sections due to flow separation, the resulting pressure loss should still be negligible compared to the overall pressure drop. However, pressure losses up to about 20% were measured for the sudden transition sections in our microdevices, which cannot be neglected. Therefore, flow separation alone is not sufficient to explain the pressure loss reported in this work, and further studies are required in order to understand such flows in microsystems.

7. Conclusions

Microdevices consisting of pairs of microchannels connected in series via transition sections with varying included angle and integrated with pressure sensors have been successfully fabricated and tested. The measured mass flow rate decreases with increasing included angle, reaching a minimum of about 65% of the theoretical value for a sudden transition. The mass flow rate in the expansion mode was only marginally lower than the contraction flow rate. Pressure distribution measurements along the straight segments of the devices show pressure losses across the transition sections, which cannot be predicted analytically. Consistent with the flow rate measurements, the pressure loss increases with increasing included angle. Indeed, accounting for these losses, the corrected values of the mass flow rates and the corresponding streamwise pressure distributions agree well with the experimental data. The magnitude of the pressure loss is significantly higher than the dynamic pressure. Therefore, it is more

https://doi.org/10.1017/S0022112002008030 Published online by Cambridge University Press

convenient to express it in terms of equivalent length. Pressure measurements around the transition sections are not sufficient to provide a clear picture of the flow patterns. However, even if they can be interpreted as an indication to flow separation from the sharp corners of the transition section, the large pressure drop cannot be the result of only flow separation since the kinetic energy of the flow is negligible compared to the driving pressure drop. Clearly, this is only the first attempt to study minor losses in microsystems and more work is required.

The work is supported by the Hong Kong Research Grant Council through RGC grant HKUST6012/98E.

REFERENCES

Arkilic, E. B., Schmidt, M. A. & Breuer, K. S. 1997 Gaseous slip flow in long microchannels. *J. Microelectromech. Syst*. **6**, 167–178.

Benedict, R. P. 1980 *Fundamentals of Pipe Flow*. Wiley.

van den Berg, H. R., ten Seldam, C. A. & van der Gulik, P. S. 1993 Compressible laminar flow in a capillary. *J. Fluid Mech*. **246**, 1–20.

Beskok, A., Karniadakis, G. E. & Trimmer, W. 1996 Rarefaction and compressibility effects in gas microflows. *Trans. ASME: J. Fluids Engng* **118**, 448–456.

Harley, J. C., Huang, Y., Bau, H. H. & Zemel, J. N. 1995 Gas flow in micro-channels. *J. Fluid Mech*. **284**, 257–274.

Ho, C. M. & Tai, Y. C. 1998 Micro-electro-mechanical systems (MEMS) and fluid flows. *Annu. Rev. Fluid Mech*. **30**, 579–612.

Lee, W. Y., Lee, S. Y. K., Wong, M. & Zohar, Y. 2000 Microchannels in series with gradual contraction/expansion. *Proc. Intl Mech. Engng Congr. & Exposition*, MEMS-vol. 2, pp. 467–472.

Lee, S. Y. K., Wong, M. & Zohar, Y. 2001*a* Pressure losses in microchannels with bends. *Proc. 14th Intl Micro Electro Mech. Systems Conf. MEMS'01*, pp. 491–494.

Lee, W. Y., Wong, M. & Zohar, Y. 2001*b* Flow separation in constriction microchannels. *Proc. 14th Intl Micro Electro Mech. Systems Conf. MEMS'01*, pp. 495–498.

Lee, S. Y. K., Wong, M. & Zohar, Y. 2001*c* Characterization of a mixing layer microdevice. *Proc. 11th Intl Conf. Solid-State Sensors and Actuators, Transducers'01*, pp. 1206–1209.

Li, X., Lee, W. Y., Wong, M. & Zohar, Y. 2000 Gas flow in constriction microdevices. *Sensors Actuat*. A **83**, 277–283.

Liu, J. Q., Tai, Y. C., Lee, J. J., Pong, K. C., Zohar, Y. & Ho, C. M. 1993*a* In situ monitoring and universal modeling of sacrificial PSG etching using hydrofluoric acid. *Proc. 6th IEEE Workshop on Micro Electro Mech. Systems, MEMS'93*, pp. 71–76.

Liu, J. Q., Tai, Y. C., Pong, K. C. & Ho, C. M. 1993*b* Micro-machined channel/pressure sensor systems for micro flow studies. *Proc. 7th Intl Conf. Solid-State Sensors and Actuators*, Transducers'93, pp. 995–999.

Meinhart, C. D., Wereley, S. T. & Santiago, J. G. 1999 PIV measurements of a microchannel flow. *Exps Fluids* **27**, 414–419.

Santiago, J. G., Wereley, S. T., Meinhart, C. D., Beebe, D. J. & Adrian, R. J. 1998 A particle image velocimetry system for microfluidics. *Exps Fluids* **25**, 316–319.

Schlichting, H. 1979 *Boundary Layer Theory*, 7th edn. McGraw–Hill.

Wu, S., Mai, J., Zohar, Y., Tai, Y. C. & Ho, C. M. 1998 A suspended microchannel with integrated temperature sensors for high-pressure flow studies. *Proc. 11th IEEE Workshop on Micro Electro Mech. Systems, MEMS'98*, pp. 87–92.

https://doi.org/10.1017/S0022112002008030 Published online by Cambridge University Press